Elucidating the Mechanistic Origin of a Spin-State Dependent FeNx-C Catalyst toward Organic Contaminant Oxidation via Peroxymonosulfate Activation

ZHANG, Bofan, LI, Xianquang, AKIYAMA, Kazuhiko, BINGHAM, Paul <http://orcid.org/0000-0001-6017-0798> and KUBUKI, Shiro

Elucidating Mechanistic Origin of Spin-Sate Dependent FeN_x-C Catalyst towards Organic Contaminants Oxidation via Peroxymonosulfate Activation

Bofan Zhang[1, †, *], Xianquan Li[2, †], Kazuhiko Akiyama[1], Paul A. Bingham[3], Shiro Kubuki[1]

[1]Department of Chemistry, Tokyo Metropolitan University, Tokyo 192-0397, Japan

[2]Dalian Institute of Chemical Physics, Chinese Academy of Sciences, Dalian 116023, China

[3]College of Business, Technology and Engineering, Sheffield Hallam University, Howard Street, Sheffield S1 1WB, UK

*Corresponding author: Bofan Zhang

E-mail: 15054218031@163.com (B.F. Zhang)

[†] These authors contributed equally

Abstract

Atomically dispersed metal on nitrogen-doped carbon matrices have delivered extensive interest in the removal of refractory organic pollutants. However, thorough exploration of the particular structure for each active site and specific effects of these sites still remains elusive. Herein, a Fe-pyridinic N_4 structure in a single-atom catalyst (FeN_x-C) was constructed using a facile pyrolysis strategy and exhibited superior catalytic activity in peroxymonosulfate (PMS) activation towards organic contaminants oxidation. The various Fe-species and relative amounts of each Fe site in the FeN_x-C catalyst were validated using X-ray absorption spectroscopy and ^{57}Fe Mössbauer spectroscopy, which show critical dependencies on the precursor ratio and calcination temperature. The positive correlations between relative content of high-spin state species (Fe^{II} and Fe^{III}) and catalytic performance were found to determine the reactive species generation and electron-transfer pathway in the FeN_x-C/PMS system. Moreover, catalytic performance and theoretical calculation results revealed that the Fe^{II}-N_4 in high spin state (S=2) tends to activate PMS to form sulfate and hydroxyl radicals via a one-electron transfer process, while the Fe^{III}-N_4 moiety (S=5/2) is prone to high-valent iron species generation with lower free energy. Benefiting from finely-tuned active sites, a single-atom FeN_x-C catalyst achieved favorable applicability in actual wastewater treatment with efficient resistance of common water matrix. The present work advances the mechanistic understanding of spin-state-dependent persulfate activation in single-atom catalysts and provides guidance to design superior catalyst based on spin-state descriptions.

Keywords: refractory organic pollutant, PMS activation, single iron atom, spin state, wastewater

Synopsis: A novel and precise spin-state dependent mechanism for wastewater treatment via peroxymonosulfate activation using single-atom Fe−N moieties was first proposed.

Introduction

The extensive use of antibiotics, pharmaceuticals, organic dyes and industrial chemicals has released increasing amounts of organic contaminants in the environment, posing a great threat to the ecological environment and human beings[1]. Reactive oxygen species-based advanced oxidation processes (AOPs) have exhibited significant potential in the broadband abatement of refractory pollutants in aqueous systems[2, 3]. Among these, persulfate-mediated Fenton-like processes including peroxymonosulfate (PMS) and peroxydisulfate (PDS) are attracting enormous interest owing to the generated highly oxidative oxygen species such as sulfate radicals, hydroxyl radicals and superoxide radicals[4]. By cleaving O-O bonds in PMS molecules via electron and energy transfer processes, the most commonly reactive species of sulfate radicals (E^0 ($SO_4^{\bullet-}/SO_4^{2-}$)) = 2.60~3.10 V_{NHE}) and hydroxyl radicals (E^0 ($^{\bullet}OH/OH^-$)) = 1.90~2.70 V_{NHE}) can be formed and further attack organic compounds[5]. Different from hydrogen peroxide (H_2O_2), PMS can also directly oxidize pollutants without radical participation[6]. However, the relatively low steady-state concentration of these species and rapid consumption by impurity substances in water and wastewater still limit PMS activation and decontamination efficiency.

Among various transition metals (Co, Fe, Cu and Mn), Fe-based Fenton-like catalysts have developed extensive and persistent interest owing to their low toxicity and cost, efficient ability and environmental sustainability[7]. Recently, the atomically dispersed single-atom catalysts (SACs) have exhibited promising potential in advanced

oxidation processes by virtue of the high degree of dispersion of metal sites, single-atom utilization, distinct electronic structure and excellent catalytic capacity[8-10]. For instance, Gao and co-workers[11] prepared single iron atoms via a cascade anchoring method as a superior catalyst to activate PMS toward bisphenol A degradation. Guan et al.[12] also demonstrated that single Fe atoms dispersed on carbon nanotubes showed excellent and selective reactivity for organic contaminants over a wide pH range for which FeN_4=O intermediate was the predominant oxidant over Fe-N_x sites. Despite the process of iron single atom in Fenton-like reaction, the catalytic mechanism behind reactive species generation and active sites is still under clarified.

It is well known that catalytic ability of SACs is strongly correlated with transition metal species, especially Fe-N_x moieties, which is at the heart of most Fenton-like reactive sites. Very recently, the transition metal sites with different spin states were considered as important aspects for explaining the excellent catalytic performance[13]. For instance, Long et al[14]. reported that Co−N−CNTs catalyst with a high spin state favored the PMS adsorption and promoted oxidation ability towards pollutant degradation. Jiang et al[15]. demonstrated that electronic spin moment is nearly linear related to the catalytic capacity of Fe-SACs during ORR reaction. Although recent processes have proposed that spin states played essential roles in catalysis process, the exact identity of the structure for each iron-based species with different spin states, their specific effect in Fenton-like reactions and in-depth mechanisms behind $Fe^{IV/V}$=O and radical species generation are still urgently in need of exploration and clarification.

Herein, a single-iron atom catalyst with Fe-N_x configuration was fabricated using a one-step pyrolysis process. The single-atomically dispersed iron species on nitrogen-doped carbon and Fe-pyridinic N_4 moiety were verified as the main active structure by a series of analytical techniques and density functional theory (DFT) calculations. In contrast to previous research, five specific iron-based species with different spin states in FeN_x-C catalysts were finely tuned and clearly observed by XAS and ^{57}Fe Mössbauer spectroscopy. During PMS activation and bisphenol A oxidation, only two of these species (high-spin Fe^{II} S=2 and Fe^{III} S=5/2) significantly contributed to the efficient Fenton-like catalytic performance. The exact process for free radicals and high valent species generation by reactive high-spin Fe^{II}/Fe^{III} was systematically explored and proposed. This work provides a novel and deeper understanding of the particular role for each iron site toward PMS activation and inspires oriented regulation and design of superior catalysts for future environmental remediation.

Experimental Section

Details of all chemicals, materials and preparation methods are listed in the Supporting Information.

Results and discussion

Structural analysis of catalysts

The synthesis procedure of FeN_x-C catalysts was demonstrated in Figure 1a via a one-step pyrolysis strategy. The optimal precursor ratio was fixed at 1:5 based on the catalytic capacity (vide infra). Three different temperatures (500, 600, 700ºC) were

selected to prepare FeN_x-C materials and the chemical structures of this series of catalysts were systematically explored. As shown in Figure S1, the X-ray diffraction pattern (XRD) of the FeN_x-C-600 sample exhibited only two representative diffraction peaks located at 27.5 and 44.5º, which were assigned to the graphitic carbon (JCPDS No. 46-0945). It is worth noting that no additional peaks corresponding to metallic iron or iron oxides were detected, excluding the existence of large crystalline iron-based nanoparticles. Distinctly different from sample FeN_x-C-600, sample FeN_x-C-700 showed obvious diffraction peaks from Fe_3C phase. TEM and HRTEM images clearly show the presence of plenty of small nanoparticles (3~5 nm) in FeN_x-C-700 catalysts (Figure S5), while no visible particles or clusters can be observed in FeN_x-C-600 samples (Figure 1b). Numerous bright spots with high density dispersed over the N-C matrix were clearly observed in high-angle annular dark-field scanning transmission electron microscopy (HAADF-STEM) images, validating the formation of atomic iron atom in FeN_x-C-600 sample. Energy dispersive X-ray spectrometry (EDX) elemental mapping reveals the highly homogenous distribution of Fe and N elements supported by the C-N substrate layer. Moreover, the Raman spectra show only two characteristic bands at 1348 and 1580 cm^{-1} corresponding to the defects and planar motion of sp^2-hybridized carbon[16] (Figure S6). The relatively high I_D/I_G ratios demonstrate the defect-rich structures in all as-synthesized catalysts[17]. The type-IV N_2 adsorption-desorption isotherm curves and correlative pore distributions (Figure S7) corroborated the presence of micro- and mesopores in the catalysts and the specific surface areas (Table

S2) gradually increase with increasing the pyrolysis temperature.

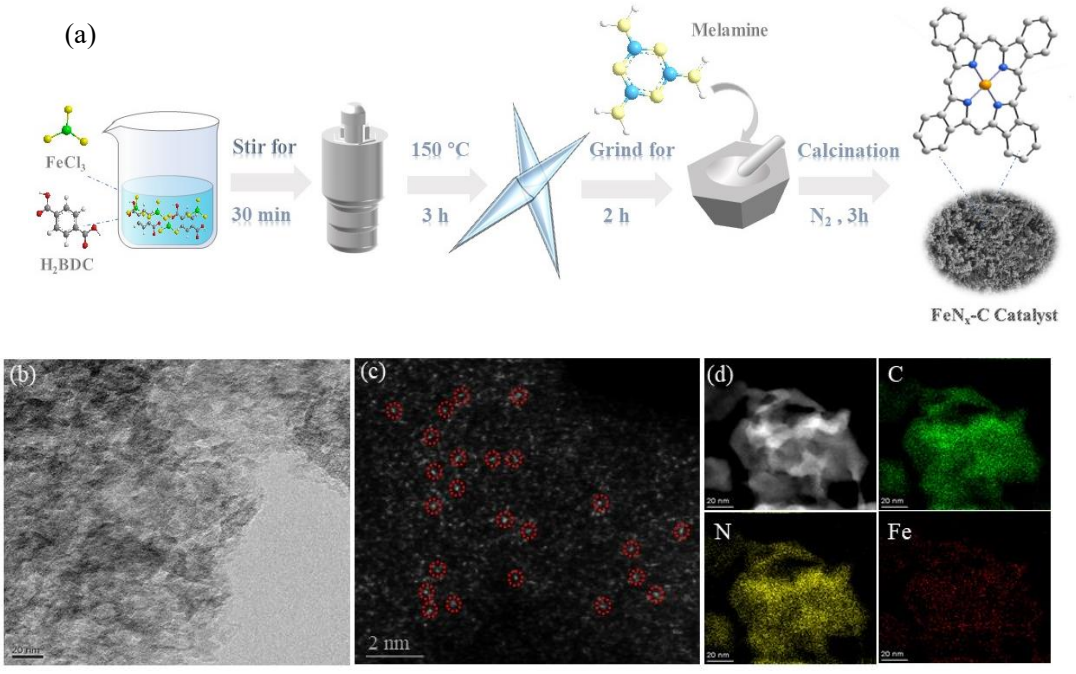

Figure 1. (a) Synthesis process of FeN_x-C catalysts; (b) TEM images; (c) HAADF-STEM image and (d) energy-dispersive X-ray mapping of FeN_x-C-600 catalyst

Chemical state and coordination environment of FeN_x-C catalyst

The chemical state and local coordination environment are essential to the exploration of catalytic reaction. The Fe 2p XPS spectra of FeN_x-C catalysts (Figure S8) revealed two characteristic peaks at ~710 and 724 eV, assigning to Fe $2p_{3/2}$ and Fe $2p_{1/2}$[18]. As depicted in Figure 2a and Figure S10, the Fe K-edge X-ray absorption near edge structure (XANES) spectrum of sample FeN_x-C-600 indicated the energy absorption threshold (edge) energy is located between those of Fe foil and Fe_2O_3 references, indicating that the Fe atoms in the FeN_x-C-600 sample possess a positive charge between Fe^0 and Fe^{3+}. It can be found that XANES spectrum of sample FeN_x-C-600 was very similar to the FePc reference, which might be derived from the

predominance of Fe-N_4 coordination sites in the FeN_x-C-600 sample. The Fourier transform (FT)- extended X-ray absorption fine structure (EXAFS) curve of sample FeN_x-C-600 exhibited only a strong peak at ~1.5 Å (Figure 2b), corresponding with the Fe-N configuration[19]. The fitting parameters of the first coordination shell illustrated an average Fe-N coordination number of 4.1 and an average Fe-N bond length of 2.06 Å. To further confirm the combination environment, possible Fe-N_x coordination models including pyridinic N, pyrrolic N and graphitic N were explored using DFT calculations. As shown in Figure S11, the lowest formation energy was found in the structure of Fe-pyridinic N_4, signifying that pyridinic N is more conducive to occupying the isolated Fe atoms with a four-coordinated site. Based on the DFT calculations and EXAFS results, Fe single atoms coordinated with an average of four pyridinic N atoms is the main configuration in FeN_x-C catalysts.

^{57}Fe Mössbauer spectroscopy is an excellent technique for identifying different iron-based materials via recoil free absorption of γ-rays using ^{57}Fe nuclei. Our previous study showed that the ^{57}Fe Mössbauer spectrum for pristine MOF precursor was composed of one doublet consistent with 100% Fe^{III} species in an octahedral geometry[20]. After calcination at different temperatures, the ^{57}Fe Mössbauer spectra for FeN_x-C catalysts indicated the presence of different Fe species and coordination environment (Figure 2c-f and Table S7). Specifically, the Mössbauer spectra for both samples FeN_x-C-500 and FeN_x-C-600 can be only fitted with doublet and no singlet and sextet, excluding the existence of zero-valence Fe crystalline phases. On the contrary, not only

169 doublets but also singlets and sextets assigned to Fe^0 and Fe_3C species[21] were clearly
170 detected in the FeN_x-C-700 sample, which is in good accordance with the results of
171 XRD and XPS. For the FeN_x-C-500 sample, the two doublets with larger IS (isomer
172 shift, > 0.80 mm/s) and QS (quadrupole splitting) values, can be assigned to the high-
173 spin Fe^{II} species (S=2)[21]. The spectrum for sample FeN_x-C-600 can be fitted robustly
174 with three different doublets (D1, D2, D3). Among these, the D1 exhibited similar
175 parameters to the doublet in the spectrum for sample FeN_x-C-500, and is assigned to
176 high-spin Fe^{II}-N_4 sites (S=2). D2, with a relatively low QS value (0.3~1.0 mm/s) and
177 an IS value of ~0.34 mm/s was ascribed to high spin Fe^{III}-N_4 sites (S=5/2) with an
178 octahedral structure due to the pulling force between Fe atoms and N_4 plane[22, 23].
179 Different from D2, D3 exhibited a similar isomer shift value (~0.37 mm/s) but a much
180 higher QS value (~1.67 mm/s), which can be assigned to low spin Fe^{III}-N_4 species
181 (S=1/2)[24]. In the spectrum for the FeN_x-C-700 sample, approximately 22.0% high-spin
182 Fe^{III} (S=5/2) was still preserved, suggesting the relative stability of this structure at
183 higher pyrolysis temperatures. Additionally, a similar IS value and larger QS value (D2)
184 than for high-spin Fe-N_4 structures attributed to the appearance of medium-spin ferrous
185 species (S=1), which is close to the configuration of ferrous iron phthalocyanine.
186 Concurrently, iron carbide and zero valent iron nanoparticles are formed and aggregated,
187 accompanying the destruction of the low-spin ferric structure, which is consistent with
188 TEM images and XRD patterns. To further explore the coordination of iron and nitrogen
189 in sample FeN_x-C-600, low temperature ^{57}Fe Mössbauer spectroscopy was performed

at 77K (Figure 2f). Notably, both room temperature and low temperature ^{57}Fe Mössbauer spectra were devoid of any singlet or sextet assignable to nanometer-sized iron particles, ruling out the existence of iron oxides, iron carbide and zero-valent irons species in the FeN_x-C-600 catalyst[25]. On the basis of these results, it can be concluded that atomically dispersed iron atoms coordinated with four pyridinic nitrogen atoms in the FeN_x-C catalyst was successfully fabricated.

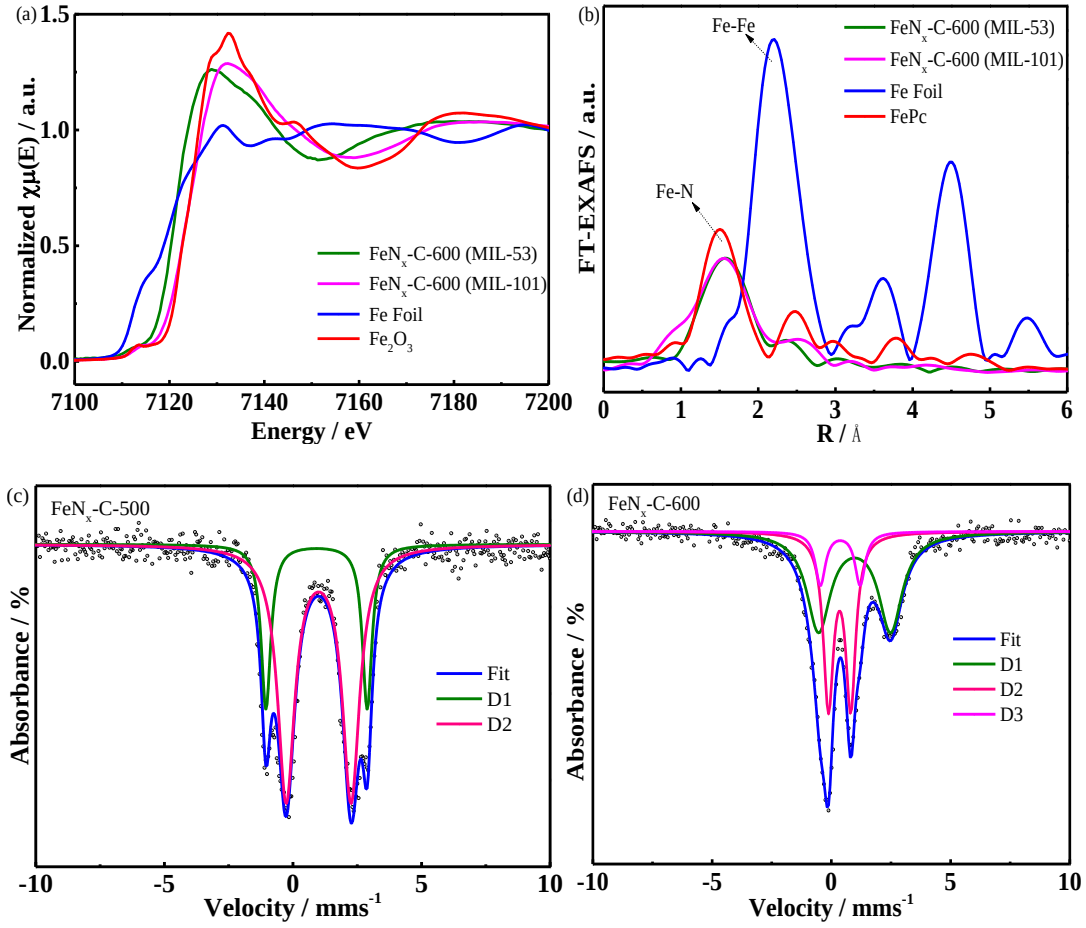

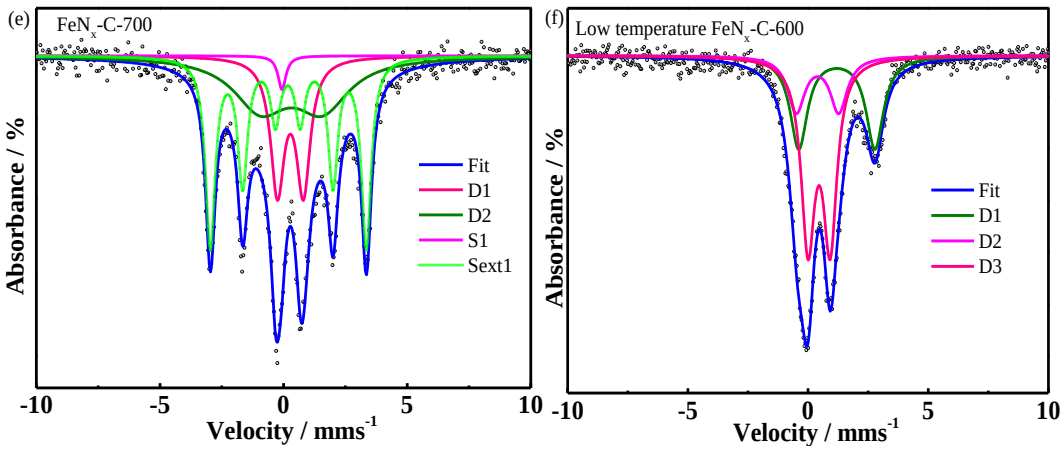

Figure 2. (a) K-edge XANES spectra of sample FeN_x-C-600, Fe_2O_3, Fe foil, FePc, (b) Fourier transforms of the k^3-weighted K-edge EXAFS spectra of sample FeN_x-C-600, Fe foil, FePc, (c-f) Room temperature and low temperature ^{57}Fe Mössbauer spectra of samples FeN_x-C-500/600/700

Evaluation of catalytic activity of FeN_x-C catalysts

The adsorption and decomposition toward bisphenol A (BPA) were evaluated using as-synthesized FeN_x-C catalysts. As depicted in Figure 3a, PMS alone and NC catalyst exhibited negligible activity toward BPA decomposition. In comparison with sample FeN_x-C-600 (99.5%), only 16.9% and 59.5% of BPA were removed by FeN_x-C-500 and FeN_x-C-700, respectively. The pseudo-first-order kinetic rate constant of sample FeN_x-C-600 exceeded those of samples FeN_x-C-500 and FeN_x-C-700 by factors of 16.23 and 9.92, respectively (Figure S15a). Moreover, the precursor ratio (Fe-MOF/melamine) at 1:5 exhibited a more rapid BPA removal than the other two mixing ratios (1:3 and 1:7, Figure S14c). The distinct difference in the Fenton-like ability between these FeN_x-C catalysts may be ascribed to the differences in surface area and pore structure, different Fe-species (Fe^0, Fe_3C, Fe-N, Fe-O, etc.) and iron coordination environments[26]. To better understand the relationship between reactivity and surface properties, a specific activity

(*k*-specific), through normalizing the rate constant by the catalyst concentration and specific surface area[11], is applied to reveal the truly intrinsic capacity of FeN_x-C catalysts. Notably, the *k*-specific value of sample FeN_x-C-600 (0.013 L m^{-2} min^{-1}) is 2.0 and 22.8 times higher than for samples FeN_x-C-500 (0.0065 L m^{-2} min^{-1}) and FeN_x-C-700 (0.00057 L m^{-2} min^{-1}), as well as those previously reported Fenton-like catalysts (Table S5), highlighting the superior catalytic performance of single iron atom decorated catalyst for PMS activation. Furthermore, more than 90% of BPA and phenol degradation can be removed, while only 14.3% of carbamazepine (CBZ), 48.5% of methylene blue (MB) and 44.2% Rhodamine B (RhB) were totally decomposed into carbon dioxide and water (Figure S13b-d), implying a certain level of selectivity towards different aromatic organic pollutants decontamination. Moreover, Figure 3b-c showed that the FeN_x-C-600/PMS system could maintain a stable and superior catalytic ability not only in the presence of various anion ions but also for the degradation of BPA in tap water and actual wastewater, indicating a robust resistance to the background matrix. These phenomena indicated that there might be other dominantly reactive oxidizing species instead of radicals in the FeN_x-C-600/PMS system. Apart from degradation efficiency, approximately 75% of total organic carbon (TOC) can be totally removed within 30 min, indicating outstanding decomposition capacity. The detailed decomposition intermediates of BPA in treated solution were detected using mass spectrometry and the possible degradation pathway was correspondingly proposed (Figure S16-17), implying the superior catalytic capacity of FeN_x-C-600 catalyst.

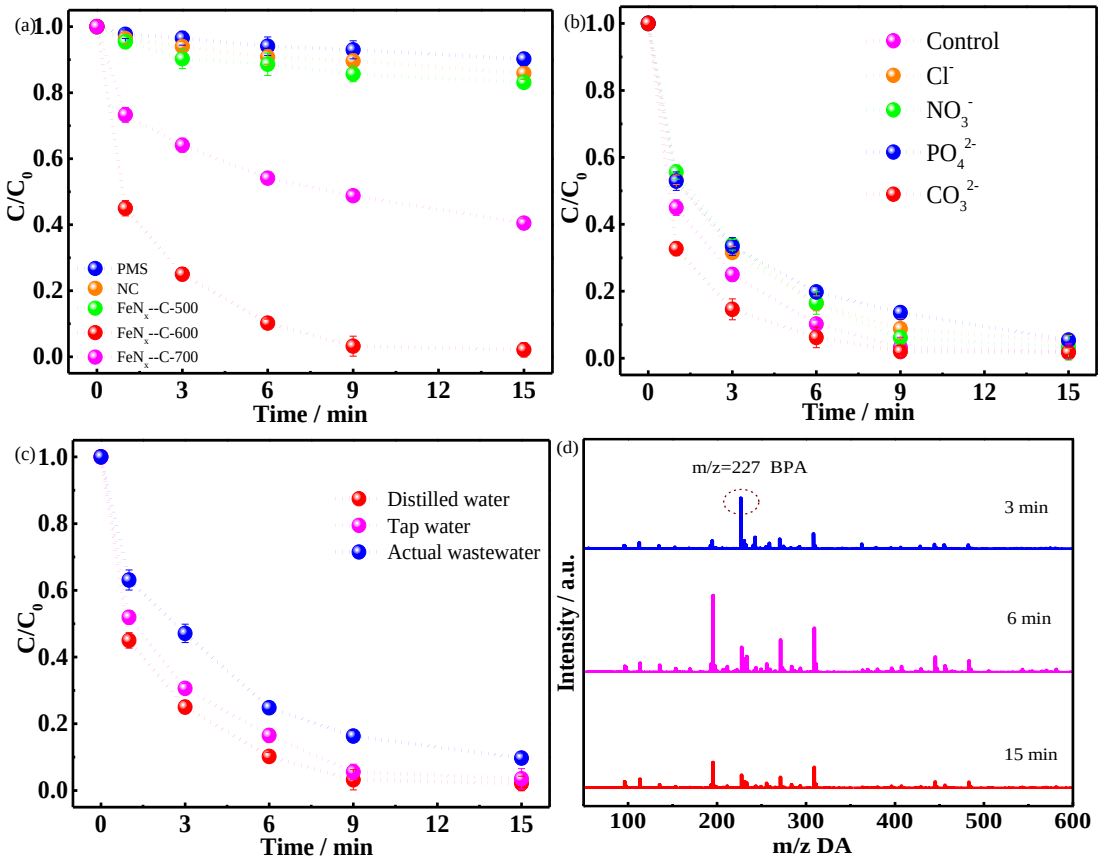

Figure 3. (a) Kinetics of BPA degradation via PMS activation with as-synthesized catalysts; (b) Influence of various anions on BPA degradation in the FeN_x-C-600/PMS system; (c) Kinetics of BPA degradation in tap water and actual wastewater via PMS activation with FeN_x-C-600 catalyst; (d) Mass spectrometry chromatogram for BPA degradation in FeN_x-C-600/PMS system. Reaction conditions: catalyst dosage = 0.2 g/L, $[PMS]_0$ = 0.50 mM, $[BPA]_0$ = 20 mg/L, pH_0 = 6.5, $[Cl^-]_0$ = $[NO_3^-]_0 = [PO_4^{2-}]_0 = [CO_3^{2-}]_0$ = 10.0 mM

Identification of active species and sites

To explore the contribution of radical species in the FeN_x-C-600/PMS system, scavenging experiments and electron paramagnetic resonance (EPR) spectroscopy measurements were conducted. Herein, methanol (MeOH) and tert-butyl alcohol (TBA) were chosen as quenchers for scavenging •OH/$SO_4^{\bullet-}$ and •OH species, respectively[27].

As depicted in Figure S18, the MeOH, at the concentration 400 times of PMS, exhibited a slight inhibition of BPA degradation, demonstrating that •OH/$SO_4^{\bullet-}$ are not the major active species. Moreover, the insignificant inhibition effect of TBA further supported this hypothesis. As shown in Figure 4, no EPR signal was detected with catalyst alone. In contrast, an intensive signal from 5,5-dimethyl-1-pyrroline N-oxide DMPO-•OH adduct and DMPO-$SO_4^{\bullet-}$ adduct appeared after 5 min in the FeN_x-C-600/PMS system compared with PMS alone, implying that the generated •OH/$SO_4^{\bullet-}$ radicals do contribute to BPA decomposition but they are not the dominant oxidant species during the Fenton-like reaction. In addition to the singlet oxygen, triplet signals with similar intensity of TEMPO adduct (2,2,6,6-tetramethyl-4-piperidine-N-oxyl) were observed for PMS alone and the FeN_x-C-600/PMS system after 5min, excluding the formation of $^1O_2$ during PMS activation and BPA degradation. Moreover, the weak intensity of DMPO-$O_2^{\cdot-}$ signals in EPR spectra (Figure S18c) was similar to that of PMS alone system, further excluding the formation of $O_2^{\cdot-}$ radicals in FeN_x-C-600/PMS system.

The N-doped carbon and Fe atoms coordinated with N-doped carbon material, have been reported to play essential roles in Fenton-like reactions[28]. As expected, the addition of oxalate evidently depressed the catalytic performance (Figure S19a), verifying the important role of iron sites for PMS activation and pollutant decomposition. Furthermore, DFT calculations were performed to explore PMS adsorption on these possible catalytic sites. As shown in Figure 4c, the adsorption energy on Fe-pyridinic N_4-C, pyridinic N-C, Fe-pyrrolic N_4-C, pyrrolic N-C and Fe-

graphitic N_4-C were calculated to be -1.471, -0.729, -0.932, -0.455 and -0.174 eV, respectively. The O-O bond length (l_{O-O}) in PMS was 1.562, 1.438 and 1.490 Å after adsorbing on the Fe-pyridinic N_4-C, Fe-pyrrolic N_4-C, and Fe-graphitic N_4-C, respectively, which were obviously elongated compared with pure PMS molecules (1.410 Å)[11]. It is noted that Fe-pyridinic N_4-C interacts more strongly with HSO_5^- in PMS molecules compared with other configuration models due to the larger adsorption energy and longer O-O bond length. Moreover, the order of the Bader charge followed Fe-pyridinic N_4 > Fe-pyrrolic N_4 > pyridinic N_4 > pyrrolic N_4 > graphitic N_4 > Fe-graphitic N_4 (Figure 4c), further confirming that PMS molecule is prone to bond with Fe-pyridinic N_4 moiety rather than nitrogen doped carbon material, which obviously accelerated the charge transfer in the FeN_x-C/PMS system. The control homogenous experiments with the addition of $FeCl_2$ and $Fe(NO_3)_3$ (1.87 μmol, the equal Fe content of sample FeN_x-C-600) were carried out (Figure S19b). As expected, the negligible effects of $FeCl_2$ and $Fe(NO_3)_3$ completely validate the reactive sites for this Fenton-like reaction are Fe-pyridinic N_4 moiety and not Fe ions. Additionally, acid etching treatment of FeN_x-C-600 catalyst was performed to remove the possible existence of surface Fe clusters or tiny nanoparticles rather than Fe-N_x species. With soaking in 2M HCl 60 ºC for 3h, the negligible change in XRD pattern, TEM images and insignificant suppression of BPA removal rate (Figure S20) validate the dominant composition and active site of Fe-N_x in the FeN_x-C-600/PMS system.

The previous studies reported Fe^{III}/Fe^{II} single atom attached to various carbon

materials can efficiently activate PMS or H_2O_2 to generate high-valent iron species (marked as HFeS)[29-31]. Considering the faint contribution of $SO_4^{\bullet-}$/•OH radicals, the confirmation of HFeS becomes indispensable in the FeN_x-C-600/PMS/BPA system. To quantitatively analyze the HFeS species, methyl phenyl sulfoxide (PMSO) and methyl phenyl sulfone ($PMSO_2$) MS spectrometry were conducted and the corresponding spectra are illustrated in Figure S21. It can be clearly observed that abundant $PMSO_2$ was detected and the intensity of $PMSO_2$ gradually increases with time, and finally levels out at a yield of around 75%. Furthermore, ^{18}O isotope-labeled products were detected using ultra-performance liquid chromatography coupled with high resolution time-of-flight mass spectrometry (UPLC-TOF-MS) via the oxygen atom exchange process between $H_2{}^{18}O$ and high valent iron species (Figure S21 g-j). Two characteristic peaks observed at m/z 157.0321 and 159.0361 in the MS spectrum are assigned to the $PMS^{16}O^{16}O$ and $PMS^{16}O^{18}O$. Moreover, two prominent peaks with m/z 78.9853 and 80.9894 represented the characteristic fragments of $PMS^{16}O^{16}O$ ($[M-C_6H_5]^+$) and $PMS^{16}O^{18}O$ ($[M-C_6H_5]^+$) can be also detected in FeN_x-C/PMS system. Contrarily, only fragment of $PMS^{16}O^{16}O$ but no $PMS^{16}O^{18}O$ was detected in PMS alone system, verifying the successful integration of ^{18}O to $PMSO_2$ using as-prepared FeN_x-C catalyst[32, 33]. On the basis of these analysis, the relatively high selectivity towards phenolic organic pollutants and the significant inhibition of various anion ions can be reasonably explained by the electrophilic addition reaction via dominant HFeS species.

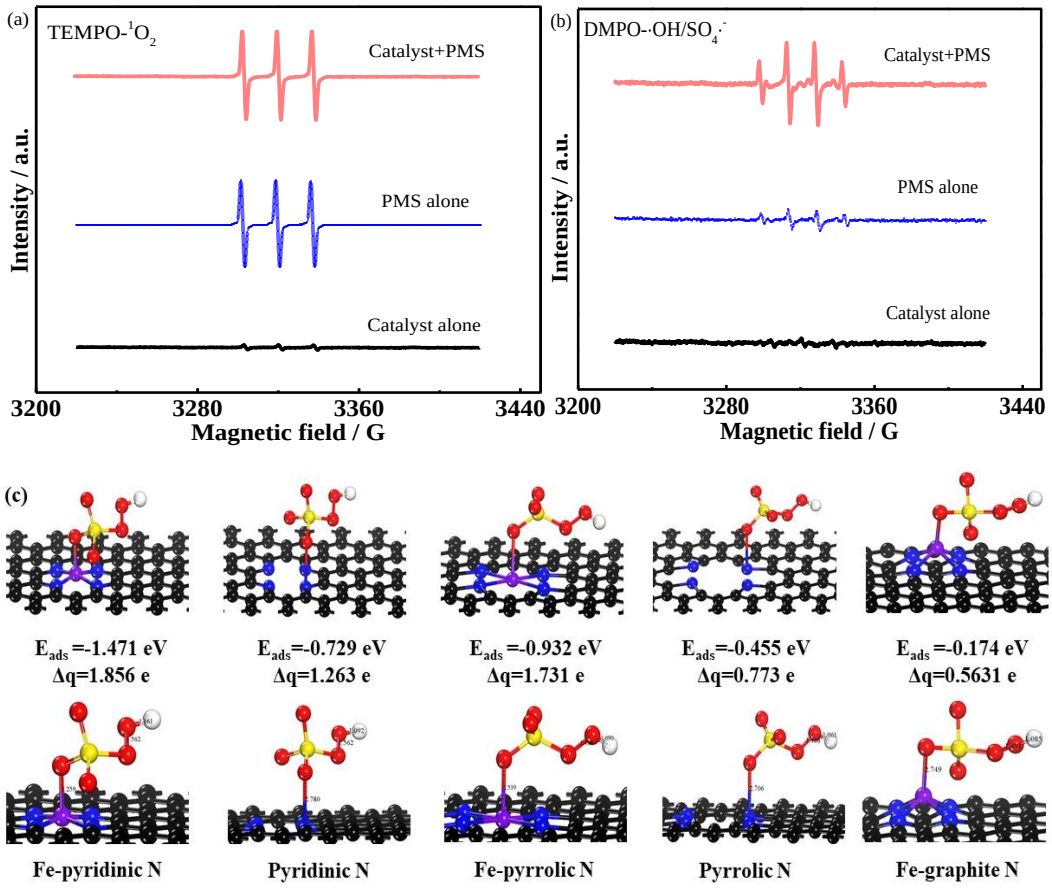

Figure 4. (a) TEMP-trapped EPR spectra for $^1O_2$; (b) DMPO-trapped EPR spectra of $SO_4^{\bullet-}$/ •OH; (c) The adsorption energy on different FeN_x-C and N-C sites and the corresponding O-O bond length in PMS and Bader charge after PMS adsorption. Reaction conditions: catalyst dosage = 0.2 g/L, $[PMS]_0$ = 0.50 mM, $[BPA]_0$ = 20 mg/L, pH_0 = 6.5

To understand the specific reaction process in the FeN_x-C-600/PMS system, *in situ* Raman spectra were carried out. As depicted in Figure 5a, the peak located at 1060 cm^{-1} is assigned to the HSO_5^- in PMS, while the peak at 982 cm^{-1} represents the S=O bond in SO_4^{2-} with symmetric stretching vibration[34]. Notably, the I_{1060}/I_{982} value significantly decreased from 1.02 to 0.68 in the corresponding FeN_x-C/PMS system, demonstrating the rapid conversion of HSO_5^- into SO_4^{2-} via the intense interaction between PMS and Fe-N_4 sites. Moreover, the dynamic PMS concentration was detected via potassium

iodide spectrophotometry[4]. It can be observed that the PMS concentration gradually declined with increasing reaction time and the tendency was almost synchronous with the BPA degradation process (Figure 5b), amply validating the surface chemical evolution of Fe-N sites for PMS decomposition rather than adsorption.

Considering that ^{57}Fe Mössbauer spectroscopy can particularly distinguish various Fe phases with similar structure but in different oxidation and spin states, the effects of different Fe sites in FeN_4 moiety for radical generation, high-valent species formation, PMS activation and BPA decomposition were systematically investigated in this work. According to the specific catalytic activity as well as their relative content in Mössbauer spectra, the intermediate-spin Fe^{II} species (S=1) can be first excluded from being dominant species. The medium-spin configuration was caused by the interaction of central Fe ions (S=1) with four nitrogen atoms, which are bonded with the surrounding carbon atoms yielding in pseudo-6-fold-octahedral coordination of iron[35]. The fully filled $3d_z^2$ orbitals in Fe^{II} sites make it difficult to approach peroxymonosulfate and pollutant molecules. Furthermore, this intermediate-spin Fe^{II} coordination (relative amount of 32.0%) only exists in the FeN_x-C-700 catalyst, for which the specific activity was just 0.00057 L m^{-2} min^{-1}, excluding a major contribution of this specie to the Fenton-like activity. For the high-spin Fe^{II} species (S=2), its larger IS value demonstrates a higher density of 3d electrons. Although its relative amounts in samples FeN_x-C-5-500, FeN_x-C-3/5/7-600, were highest, here it did not contribute the most to BPA degradation. This is because decreasing the pyrolysis temperature to 500°C

345 improved the relative Fe content present in high-spin Fe^{II} state, without obviously
346 increasing the catalytic performance. However, considering the higher specific activity
347 compared with sample FeN_x-C-700, the high-spin Fe^{II} species in sample FeN_x-C-500
348 did provide a certain enhancement in PMS activation and BPA decomposition. This
349 might be ascribed to high-spin Fe^{II} configuration with S=2 and $3d_z^2$ orbital occupied by
350 single electron being conducive to directly activate PMS via electron transfer
351 pathways[36]. Notably, by comparing the Fenton-like activity with the relative abundance
352 of each Fe component, the superior catalytic activity of FeN_x-C catalyst closely
353 correlates with its relatively larger amount of high-spin Fe^{III} species (S=5/2), with a
354 coefficient of determination R^2 of 0.995 (Figure S22e-f). In comparison with sample
355 FeN_x-C-3-600, the higher HS Fe^{III} and lower LS Fe^{III} phase in sample FeN_x-C-5-600
356 resulted in excellent catalytic efficiency toward BPA removal, which can be also
357 identified by the FeN_x-C-7-600 catalyst. When the calcination temperature increased to
358 700 °C, the relative content of high-spin Fe^{III} in sample FeN_x-C-700 was only 22.0%,
359 far below the content in sample FeN_x-C-5-600. The relative content of high-spin
360 Fe^{III}/Fe^{II} was positively correlated with the catalytic capacity, indicating that the
361 efficiency of PMS activation and BPA oxidation was governed by the spin state of Fe-
362 N_x sites owing to the space electronic configuration differentiation in d orbitals.
363 Generally, the high-spin state of Fe-N_x sites with large magnetic moments is conducive
364 to participating in σ-bonding with PMS molecule via overlapping with O 2p orbitals[36],
365 thereby improving PMS adsorption ability, promoting the oxidation potential and

accelerating electron transfer during the Fenton-like reaction. In contrast, the structure of low-spin Fe^{III} is highly saturated and the number of unpaired electrons with the same spin direction is the smallest[23], making it difficult to be a reactive site. Moreover, the newly formed Fe_3C (44.4%) and Fe^0 (Super-paramagnetic Fe, 1.6%) in FeN_x-C-700 are unlikely to significantly improve the pollutants removal efficiency, excluding the dominant role of these species in the FeN_x-C/PMS/BPA system.

Furthermore, DFT calculations were undertaken to shed light on the pathway of PMS activation into $SO_4^{\cdot-}$, ·OH radicals and Fe(V)=O complex via the proposed Fe-pyridinic N_4 configurations with different spin-state. The energy profiles and corresponding intermediate structure were shown in Figure 5c-d. Considering that single-electron, two-electron and oxygen atom transfer pathways[37] may occur simultaneously in the FeN_x-C/PMS system, multiple binding configurations and the corresponding free energies were calculated. When the PMS molecule was adsorbed on the Fe-pyridinic N_4 sites, it can be rapidly activated and subsequently generate intermediate (II) and transition state (TS), and finally form reactive oxygen species ($SO_4^{\cdot-}$, ·OH, Fe(V)=O). As depicted in Figure 5c, the Gibbs free energies for formation of $SO_4^{\cdot-}$, ·OH radicals were much lower than the reactant, demonstrating that it is thermodynamically favorable. Among them, the most favorable active site for $SO_4^{\cdot-}$, ·OH radical formation with the lowest Gibbs free energy was high-spin Fe^{II} rather than the Fe^{III}-N_4 moiety. Contrarily, the free energy for generating high valent iron species Fe(V) by Fe^{II}-N_4 is about 0.59 and 0.64 eV, which is an endothermic process and cannot

happen automatically under ambient conditions. Different from Fe^{II}-N_4 moiety, the energy barrier for Fe(V)=O complex formation is easier to overcome by high-spin Fe^{III}-N_4 sites, which is an exothermic reaction and favorable in thermodynamics and kinetics. In other words, the high spin Fe^{III} S=5/2 and Fe^{II} S=2 sites are much more reactive to bond with PMS to generate Fe(V)=O complexes and $SO_4^{\cdot -}$, ·OH radicals, respectively, which is consistent with the experimental results.

Low temperature EPR measurement, which could provide detailed information of iron species with half-integer spin and the potential presence of high valent iron components in the redox reaction[38], was carried out at 77K. As shown in Figure 5e and Figure S23a, an isotropic signal at g=2.0034 was detected in the FeN_x-C-600/H_2O system, ascribed to the partial $3d^5$ orbitals of Fe^{III} with large zero-field splitting and unpaired electrons[39]. Notably, after mixing PMS with FeN_x-C-600 catalyst, the intensity of this signal was enhanced and exhibited a positive shift to a lower value. This phenomenon was consistent with the previous report by Dashdorj et al.,[40] likely originating the generation of Fe^{V}=O via oxidizing high-spin Fe^{III} sites (S=5/2) during PMS conversion process. Additionally, a broad isotropic signal at g=4.282 originating from rhombic high-spin ferric species was also clearly detected[38]. In comparison with the deionized water system, the increased intensity of ferric sites after addition of PMS demonstrated more production of Fe^{III} species, which are mainly derived from the redox characteristics of Fe^{II}/Fe^{III} and Fe^{III}/Fe^{V} during activation of PMS via atomically dispersed iron-N sites. Moreover, the current density displayed an obvious drop with

the addition of PMS (Figure 5f), likely ascribed to electron redistribution owing to the interaction between PMS and the surface of the catalyst. The subsequent introduction of BPA provoked a remarkable decline in current density, indicating the occurrence of electron transfer between BPA, PMS and FeN_x-C-600 catalyst.

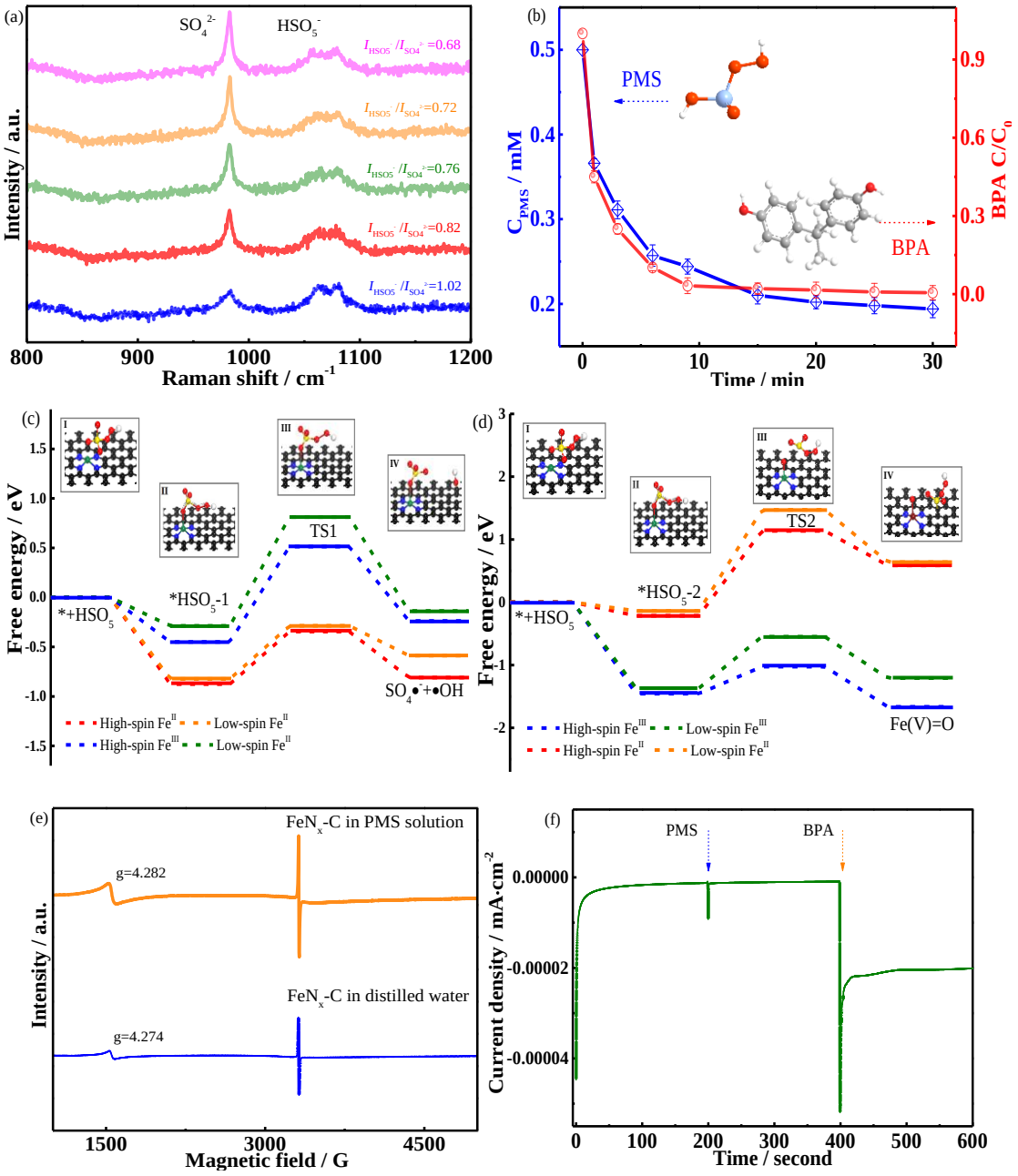

Figure 5. (a) *In situ* Raman spectra of FeN_x-C-600/PMS system measured at different reaction times; (b) Variation of PMS concentration and BPA removal rate in the FeN_x-C-600/PMS/BPA

system; (c-d) Reaction pathways of $SO_4^{\cdot -}$, ·OH radicals and Fe(V)=O generation at different spin state Fe sites; (e) EPR spectra of FeN_x-C-600 in distilled water and PMS solution under 77K; (f) Current response at the FeN_x-C-600 coated working electrode; Reaction conditions: catalyst dosage = 0.2 g/L, $[PMS]_0$ = 0.50 mM, $[BPA]_0$ = 20 mg/L, pH_0 = 6.5

On the basis of experimental results and theoretical calculations, the overall mechanism for PMS activation and pollutant oxidation using FeN_x-C catalyst was proposed in Figure 6. The PMS molecule could first react with Fe-pyridinic N_4 moieties including $Fe^{II}N_4$ and $Fe^{III}N_4$ sites to form FeN_x-$(HO)OSO_3^-$ intermediates. Due to that PMS can be decomposed via cleavage of the O-O bond, and the formed $Fe^{II}N_x$-$(HO)OSO_3^-$ was further activated to generate $SO_4^{\cdot -}$ radicals via a one-electron transfer, while the $Fe^{III}N_x$-$(HO)OSO_3^-$ could form high-valent species (Fe^{V}=O complex) via a two-electron and O-atom transfer[41]. The $SO_4^{\cdot -}$ radicals can further react with H_2O in the solution to yield ·OH. Benefiting from the effect of predominant high-valent iron species and supporting $SO_4^{\cdot -}$ and ·OH radicals, bisphenol A can be efficiently decomposed into small organic substrates, CO_2 and H_2O. Owing to the consumption of transient Fe^{V}=O complex by bisphenol oxidation, the Fe^{V} can be reduced and transformed into Fe^{III}, achieving redox circulation between Fe^{V} and Fe^{III}. After the Fenton-like reaction, the relative content of Fe^{II} and Fe^{III} remains almost unchanged, as demonstrated by ^{57}Fe Mössbauer spectroscopy (Figure S22c) and Fe 2p XPS spectroscopy (Figure S25a), demonstrating an efficient conversion of Fe^{III}/Fe^{II} and Fe^{V}/Fe^{III} in the FeN_x-C/BPA/PMS system.

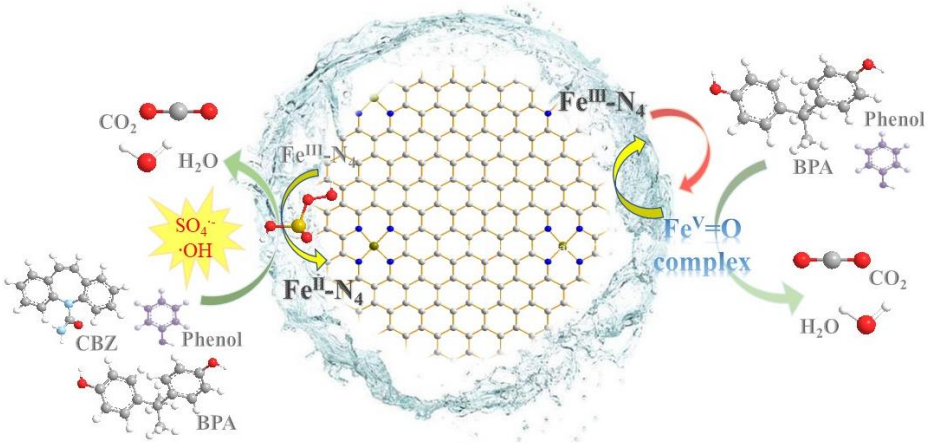

Figure 6. Proposed mechanism behind PMS activation over FeN_x-C-600 catalyst toward organic pollutants decomposition

To furnish evidence of the universal applicability of this preparation strategy and mechanistic exploration, a similarly structured Fe-MOF, named MIL-101(Fe) was chosen as a precursor to synthesize single atom catalyst using a procedure being parallel to that of the MIL-53 based FeN_x-C sample. The XRD, HRTEM, XAS results indicated the successful construction of an atomic structure model of the 101FeN_x-C catalyst (Figure S24). The ^{57}Fe Mössbauer spectra of 101FeN_x-C can be deconvoluted into three doublets based on IS and QS values (Figure S22d), which are assigned to the Fe-N_4 moieties with different local coordination structures (high-spin Fe^{II} S=2, high-spin Fe^{III} S=5/2 and low-spin Fe^{III} species S=1/2). The coordination of these three components was similar to the MIL-53 based FeN_x-C sample, indicating the existence of similar Fe single atomic structures. Notably, the relative amount of high-spin Fe^{III} is close to that in the MIL-53 based FeN_x-C, while high-spin Fe^{II} site is lower and low-spin Fe^{III} is larger than for the MIL-53 based FeN_x-C sample (Table S7). This phenomenon could explain the slightly decreased removal efficiency of BPA by sample 101FeN_x-C

(k=0.268 min^{-1}) compared with MIL-53 based FeN_x-C (k=0.357 min^{-1}), further validating the dominant role of high-spin Fe^{III} and supporting effect of high-spin Fe^{II} during the Fenton-like reaction.

In view of the durability and practicability, a continuous batch experiment was conducted. With the number of cycles increased, approximately 89.8% BPA degradation efficiency can be still achieved by sample FeN_x-C-600 (Figure S26). The total leached iron (0.37 mg/L) did not give rise to significant catalytic ability towards PMS activation and BPA degradation (Figure S26d). The XPS spectrum of sample FeN_x-C-600 indicated that the relative amounts of N and Fe slightly decreased (Figure S25), while O content increased after cyclic experiments. These results illustrate that the attenuation of removal efficiency might be ascribed to the slight loss of Fe and N content[11], resulting in a reduced number of active sites for PMS activation and pollutant degradation, which is consistent with the result of ^{57}Fe Mössbauer spectra of used catalysts (Figure S22). Furthermore, XRD pattern and FTIR spectra (Figure S26b-c) signify the highly stable crystal structure and no other Fe species aggregation on the catalyst surface. The practicability of sample FeN_x-C-600 toward BPA decontamination in tap water and realistic industrial wastewater was also tentatively evaluated. Wastewater was collected from the effluent of the Tokyo Sewerage system in Tokyo, Japan. The parameters of the wastewater were summarized in Table.S6. As depicted in Figure S26d-e, sample FeN_x-C-600 still fulfilled high removal efficiency of BPA in actual wastewater and tap water via PMS activation. Considering the extremely low

concentration of metallic ions in the wastewater sample, the outstanding catalytic performance for BPA oxidation was mainly contributed to the catalyst itself, which confirm the distinct advantage of catalyst FeN_x-C-600 in engineering to remediate actual wastewater.

Environmental Implications

A single-atom iron catalyst with Fe-pyridinicN_4 configuration was successfully synthesized using a facile pyrolysis strategy in this work. As a PMS activator, catalyst FeN_x-C-600 delivered superior catalytic activity for refractory organic pollutant decomposition, for which the specific activity was much higher than the control experiments and various previously reported heterogeneous catalysts. Moreover, the robust stability and efficient applicability in practical wastewater remediation clearly demonstrate its potential to be a candidate in future environmental remediation. The positive correlation between relative contents of high-spin state species (Fe^{II} S=2 and Fe^{III} S=5/2) and catalytic performance was strongly evidenced by ^{57}Fe Mössbauer spectroscopy and DFT calculations, which determined the reactive species generation and electron-transfer pathway in the FeN_x-C/PMS/BPA system. Therefore, a thorough understanding of the spin-state dependent mechanism for PMS activation over single Fe atoms was discerned in this work. These findings highlight in detail the exact identifies of the various iron coordination sites and the specific catalytic pathways of these sites during PMS conversion and compounds decontamination, providing valuable guidance to design strategies toward promoting catalytic capacity in future

real-world applications.

Supporting Information

Details of chemicals, synthesis and characterization of catalysts; analytic methods; XRD patterns; TG curve; SEM and TEM images; Raman spectra; N_2 adsorption-desorption isotherm; XPS, XAS and ^{57}Fe Mössbauer spectra; DFT calculation result; catalytic performance of pollutants; influence of different parameters; UPLC/MS spectra and BPA degradation pathway; scavenging test result; PMSO consumption and $PMSO_2$ generation; ERP spectra; cycling experiment; characterization of $101FeN_x$-C-600 catalyst; TOC removal efficiency; BPA degradation in actual wastewater;

Acknowledgements

This work was supported by the Tokyo Human Resources Fund for City Diplomacy (H29-1). The authors wish to acknowledge Dr Németh Zoltán, Institute of Wigner Research Centre for Physics, for his help in guiding the analysis of the X-ray absorption spectra (XAS) results of this study.

References

1. Rojas, S.; Horcajada, P. Metal–Organic Frameworks for the Removal of Emerging Organic Contaminants in Water. *Chem. Rev.* **2020,** *120*, 8378-8415.

2. Zhen, Y.; Zhu, S.; Sun, Z.; Tian, Y.; Li, Z.; Yang, C.; Ma, J. Identifying the Persistent Free Radicals (PFRs) Formed as Crucial Metastable Intermediates during Peroxymonosulfate (PMS) Activation by N-Doped Carbonaceous Materials. *Environ. Sci. Technol.* **2021,** *55*, 9293-9304.

3. Bae, G.; Chung, M. W.; Ji, S. G.; Jaouen, F.; Choi, C. H. pH Effect on the H_2O_2-Induced Deactivation of Fe-N-C Catalysts. *ACS Catal.* **2020,** *10*, 8485-8495.

4. Lee, J.; von Gunten, U.; Kim, J. H. Persulfate-Based Advanced Oxidation: Critical Assessment of Opportunities and Roadblocks. *Environ. Sci. Technol.* **2020,** *54*, 3064-3081.

5. Peng, Y.; Tang, H.; Yao, B.; Gao, X.; Yang, X.; Zhou, Y. Activation of peroxymonosulfate (PMS) by spinel ferrite and their composites in degradation of organic pollutants: A Review. *Chem. Eng. J.* **2021,** *414,* 128800.

6. Wu, L.; Li, B.; Li, Y.; Fan, X.; Zhang, F.; Zhang, G.; Xia, Q.; Peng, W. Preferential Growth of the Cobalt (200) Facet in Co@N–C for Enhanced Performance in a Fenton-like Reaction. *ACS Catal.* **2021,** *11*, 5532-5543.

7. Tang, Z.; Zhao, P.; Wang, H.; Liu, Y.; Bu, W. Biomedicine Meets Fenton Chemistry. *Chemical Reviews* **2021,** *121*, 1981-2019.

8. Jiao, L.; Jiang, H.-L. Metal-Organic-Framework-Based Single-Atom Catalysts for Energy Applications. *Chem* **2019,** *5*, 786-804.

9. Xu, J.; Zheng, X.; Feng, Z.; Lu, Z.; Zhang, Z.; Huang, W.; Li, Y.; Vuckovic, D.; Li, Y.; Dai, S.; Chen, G.; Wang, K.; Wang, H.; Chen, J. K.; Mitch, W.; Cui, Y. Organic wastewater treatment by a single-atom catalyst and electrolytically produced H_2O_2. *Nat Sustain.* **2020,** *4*, 233-241.

10. Shang, Y.; Xu, X.; Gao, B.; Wang, S.; Duan, X. Single-atom catalysis in advanced oxidation processes for environmental remediation. *Chem. Soc. Rev.* **2021,** *50*, 5281-5322.

11. Gao, Y.; Zhu, Y.; Li, T.; Chen, Z.; Jiang, Q.; Zhao, Z.; Liang, X.; Hu, C. Unraveling the High-Activity Origin of Single-Atom Iron Catalysts for Organic Pollutant Oxidation via

Peroxymonosulfate Activation. *Environ. Sci. Technol.* **2021,** *55*, 8318-8328.

12. Qian, K.; Chen, H.; Li, W.; Ao, Z.; Wu, Y. N.; Guan, X. Single-Atom Fe Catalyst Outperforms Its Homogeneous Counterpart for Activating Peroxymonosulfate to Achieve Effective Degradation of Organic Contaminants. *Environ. Sci. Technol.* **2021,** *55*, 7034-7043.

13. Shen, G.; Zhang, R.; Pan, L.; Hou, F.; Zhao, Y.; Shen, Z.; Mi, W.; Shi, C.; Wang, Q.; Zhang, X.; Zou, J.-J. Regulating the Spin State of FeIII by Atomically Anchoring on Ultrathin Titanium Dioxide for Efficient Oxygen Evolution Electrocatalysis. *Angew. Chem., Int. Ed.* **2020,** *59*, 2313-2317.

14. Miao, J.; Zhu, Y.; Lang, J.; Zhang, J.; Cheng, S.; Zhou, B.; Zhang, L.; Alvarez, P. J. J.; Long, M. Spin-State-Dependent Peroxymonosulfate Activation of Single-Atom M–N Moieties via a Radical-Free Pathway. *ACS Catal.* **2021,** *11*, 9569-9577.

15. Zhong, W.; Qiu, Y.; Shen, H.; Wang, X.; Yuan, J.; Jia, C.; Bi, S.; Jiang, J. Electronic Spin Moment As a Catalytic Descriptor for Fe Single-Atom Catalysts Supported on C_2N. *J. Am. Chem. Soc.* **2021,** *143*, 4405-4413.

16. Mineva, T.; Matanovic, I.; Atanassov, P.; Sougrati, M.-T.; Stievano, L.; Clémancey, M.; Kochem, A.; Latour, J.-M.; Jaouen, F. Understanding Active Sites in Pyrolyzed Fe–N–C Catalysts for Fuel Cell Cathodes by Bridging Density Functional Theory Calculations and ^{57}Fe Mössbauer Spectroscopy. *ACS Catal.* **2019,** *9*, 9359-9371.

17. Peng, L.; Duan, X.; Shang, Y.; Gao, B.; Xu, X. Engineered carbon supported single iron atom sites and iron clusters from Fe-rich Enteromorpha for Fenton-like reactions via nonradical pathways. *Appl. Catal., B* **2021,** *287,* 119963.

18. Zhou, Y.; Zhou, L.; Zhou, Y.; Xing, M.; Zhang, J. Z-scheme photo-Fenton system for efficiency synchronous oxidation of organic contaminants and reduction of metal ions. *Appl. Catal., B* **2020,** *279,* 119365.

19. Weon, S.; Huang, D.; Rigby, K.; Chu, C.; Wu, X.; Kim, J.-H. Environmental Materials beyond and below the Nanoscale: Single-Atom Catalysts. *ACS ES&T Engg* **2021,** *1*, 157-172.

20. Zhang, B.; Zhang, L.; Akiyama, K.; Bingham, P. A.; Zhou, Y.; Kubuki, S. Self-Assembly of Nanosheet-Supported Fe-MOF Heterocrystals as a Reusable Catalyst for Boosting

Advanced Oxidation Performance via Radical and Nonradical Pathways. *ACS Appl. Mater. Interfaces* **2021,** *13*, 22694-22707.

21. Xing, Y.; Yao, Z.; Li, W.; Wu, W.; Lu, X.; Tian, J.; Li, Z.; Hu, H.; Wu, M. Fe/Fe_3C Boosts H_2O_2 Utilization for Methane Conversion Overwhelming O_2 Generation. *Angew. Chem., Int. Ed.* **2021,** *60*, 8889-8895.

22. Sahraie, N. R.; Kramm, U. I.; Steinberg, J.; Zhang, Y.; Thomas, A.; Reier, T.; Paraknowitsch, J.-P.; Strasser, P. Quantifying the density and utilization of active sites in non-precious metal oxygen electroreduction catalysts. *Nat. Commun.* **2015,** *6*, 8618.

23. Li, J.; Ghoshal, S.; Liang, W.; Sougrati, M.-T.; Jaouen, F.; Halevi, B.; McKinney, S.; McCool, G.; Ma, C.; Yuan, X.; Ma, Z.-F.; Mukerjee, S.; Jia, Q. Structural and mechanistic basis for the high activity of Fe–N–C catalysts toward oxygen reduction. *Energy Environ. Sci.* **2016,** *9*, 2418-2432.

24. Zhu, Y.; Zhang, B.; Liu, X.; Wang, D.-W.; Su, D. S. Unravelling the Structure of Electrocatalytically Active Fe–N Complexes in Carbon for the Oxygen Reduction Reaction. *Angew. Chem., Int. Ed.* **2014,** *53*, 10673-10677.

25. Collings, I. E.; Vasiukov, D. M.; McCammon, C. A.; Dubrovinsky, L.; Cerantola, V.; Petitgirard, S.; Hübschle, C. B.; Schönleber, A.; Chernyshov, D.; van Smaalen, S.; Dubrovinskaia, N. Local Structure of Ferroic Iron Formates at Low Temperature and High Pressure Studied by Mössbauer Spectroscopy. *J. Phys. Chem. C* **2019,** *123*, 21676-21684.

26. Chen, Z.; Song, J.; Peng, X.; Xi, S.; Liu, J.; Zhou, W.; Li, R.; Ge, R.; Liu, C.; Xu, H.; Zhao, X.; Li, H.; Zhou, X.; Wang, L.; Li, X.; Zhong, L.; Rykov, A. I.; Wang, J.; Koh, M. J.; Loh, K. P. Iron Single Atom Catalyzed Quinoline Synthesis. *Adv. Mater.* **2021**, e2101382.

27. Li, H.; Zhao, Z.; Qian, J.; Pan, B. Are Free Radicals the Primary Reactive Species in Co(II)-Mediated Activation of Peroxymonosulfate? New Evidence for the Role of the Co(II)-Peroxymonosulfate Complex. *Environ. Sci. Technol.* **2021,** *55*, 6397-6406.

28. Jiang, N.; Xu, H.; Wang, L.; Jiang, J.; Zhang, T. Nonradical Oxidation of Pollutants with Single-Atom-Fe(III)-Activated Persulfate: Fe(V) Being the Possible Intermediate Oxidant. *Environ.*

Sci. Technol. **2020,** *54*, 14057-14065.

29. Liang, J.; Duan, X.; Xu, X.; Chen, K.; Zhang, Y.; Zhao, L.; Qiu, H.; Wang, S.; Cao, X. Persulfate Oxidation of Sulfamethoxazole by Magnetic Iron-Char Composites via Nonradical Pathways: Fe(IV) Versus Surface-Mediated Electron Transfer. *Environ. Sci. Technol.* **2021,** *55*, 10077-10086.

30. Dong, H.; Li, Y.; Wang, S.; Liu, W.; Zhou, G.; Xie, Y.; Guan, X. Both Fe(IV) and Radicals Are Active Oxidants in the Fe(II)/Peroxydisulfate Process. *Environ. Sci. Technol. Lett.* **2020,** *7*, 219-224.

31. Jin, Q.; Kang, J.; Chen, Q.; Shen, J.; Guo, F.; Chen, Z. Efficiently enhanced Fenton-like reaction via Fe complex immobilized on silica particles for catalytic hydrogen peroxide degradation of 2,4-dichlorophenol. *Appl. Catal., B* **2020,** *268,* 118453.

32. Zong, Y.; Guan, X.; Xu, J.; Feng, Y.; Mao, Y.; Xu, L.; Chu, H.; Wu, D., Unraveling the Overlooked Involvement of High-Valent Cobalt-Oxo Species Generated from the Cobalt(II)-Activated Peroxymonosulfate Process. *Environ. Sci. Technol.* **2020,** *54*, 16231-16239.

33. Zong, Y.; Zhang, H.; Zhang, X.; Liu, W.; Xu, L.; Wu, D., High-valent cobalt-oxo species triggers hydroxyl radical for collaborative environmental decontamination. *Appl. Catal., B* **2022,** *300*, 120722.

34. Zhang, T.; Zhu, H.; Croue, J. P. Production of sulfate radical from peroxymonosulfate induced by a magnetically separable $CuFe_2O_4$ spinel in water: efficiency, stability, and mechanism. *Environ. Sci. Technol.* **2013,** *47*, 2784-91.

35. Kramm, U. I.; Herrmann-Geppert, I.; Behrends, J.; Lips, K.; Fiechter, S.; Bogdanoff, P. On an Easy Way To Prepare Metal-Nitrogen Doped Carbon with Exclusive Presence of MeN4-type Sites Active for the ORR. *J. Am. Chem. Soc.* **2016,** *138*, 635-40.

36. Kramm, U. I.; Herranz, J.; Larouche, N.; Arruda, T. M.; Lefevre, M.; Jaouen, F.; Bogdanoff, P.; Fiechter, S.; Abs-Wurmbach, I.; Mukerjee, S.; Dodelet, J. P. Structure of the catalytic sites in Fe/N/C-catalysts for O_2-reduction in PEM fuel cells. *Phys. Chem. Chem. Phys.* **2012,** *14*, 11673-88.

37. Zhao, Y.; Deng, C.; Tang, D.; Ding, L.; Zhang, Y.; Sheng, H.; Ji, H.; Song, W.;

Ma, W.; Chen, C.; Zhao, J. α-Fe_2O_3 as a versatile and efficient oxygen atom transfer catalyst in combination with H_2O as the oxygen source. *Nat. Catal.* **2021,** *4*, 684-691.

38. Saveleva, V. A.; Ebner, K.; Ni, L.; Smolentsev, G.; Klose, D.; Zitolo, A.; Marelli, E.; Li, J.; Medarde, M.; Safonova, O. V.; Nachtegaal, M.; Jaouen, F.; Kramm, U. I.; Schmidt, T. J.; Herranz, J. Potential-Induced Spin Changes in Fe/N/C Electrocatalysts Assessed by In Situ X-ray Emission Spectroscopy. *Angew. Chem., Int. Ed.* **2021,** *60*, 11707-11712.

39. Kramm, U. I.; Herrmann-Geppert, I.; Behrends, J.; Lips, K.; Fiechter, S.; Bogdanoff, P. On an Easy Way To Prepare Metal–Nitrogen Doped Carbon with Exclusive Presence of MeN_4-type Sites Active for the ORR. *J. Am. Chem. Soc.* **2016,** *138*, 635-640.

40. Dashdorj, J.; Zvanut, M. E.; Stanley, L. J. Iron-related defect levels in $SrTiO_3$ measured by photoelectron paramagnetic resonance spectroscopy. *J. Appl. Phys.* **2010,** *107*, 083513.

41. Wang, Z.; Jiang, J.; Pang, S.; Zhou, Y.; Guan, C.; Gao, Y.; Li, J.; Yang, Y.; Qiu, W.; Jiang, C. Is Sulfate Radical Really Generated from Peroxydisulfate Activated by Iron(II) for Environmental Decontamination? *Environ. Sci. Technol.* **2018,** *52*, 11276-11284.